THE JOURNAL OF PHYSICAL CHEMISTRY C
A JOURNAL OF THE AMERICAN CHEMICAL SOCIETY

pubs.acs.org/JPCC Article

Molecular-Scale Elucidation of Ionic Charge Storage Mechanisms in Rechargeable Aluminum−Quinone Batteries

Leo W. Gordon, Ankur L. Jadhav, Mikhail Miroshnikov, Theresa Schoetz, George John, and Robert J. Messinger*

Cite This: *J. Phys. Chem. C* 2022, 126, 14082−14093 **Read Online**

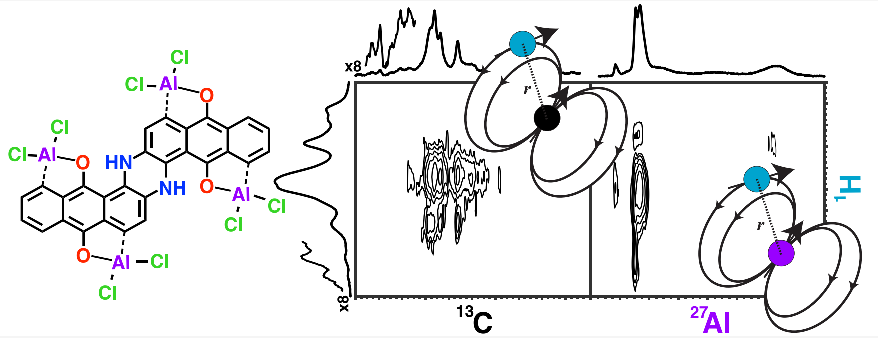

ABSTRACT: Rechargeable aluminum−organic batteries are of great interest as a next-generation energy storage technology because of the earth abundance, high theoretical capacity, and inherent safety of aluminum metal, coupled with the sustainability, availability, and tunabilty of organic molecules. However, the ionic charge storage mechanisms occurring in aluminum−organic batteries are currently not well understood, in part because of the diversity of possible charge-balancing cations, coupled with a wide array of possible binding modes. For the first time, we use multidimensional solid-state NMR spectroscopy in conjunction with electrochemical methods to elucidate experimentally the ionic and electronic charge storage mechanism in an aluminum−organic battery up from the atomic length scale. In doing so, we present indanthrone quinone (INDQ) as a positive electrode material for rechargeable aluminum batteries, capable of reversibly achieving specific capacities of ca. 200 mAh g^{-1} at 0.12 A g^{-1} and 100 mAh g^{-1} at 2.4 A g^{-1}. We demonstrate that INDQ stores charge via reversible electrochemical enolization reactions, which are charge compensated in chloroaluminate ionic liquid electrolytes by cationic chloroaluminous ($AlCl_2^+$) species in tetrahedral geometries. The results are generalizable to the charge storage mechanisms underpinning anthraquinone-based aluminum batteries. Lastly, the solid-state dipolar-mediated NMR experiments used here establish molecular-level interactions between electroactive ions and organic frameworks while filtering mobile electrolyte species, a methodology applicable to many multiphase host−guest systems.

■ INTRODUCTION

Societal demand for electrochemical energy storage is continually increasing, placing constraints on low-abundance and geopolitically scarce materials, such as lithium and cobalt.[1−3] Thus, more sustainable materials for energy storage are needed. Rechargeable aluminum metal batteries are an emerging electrochemical energy storage technology with great promise, as aluminum has a large theoretical capacity (8046 mAh g^{-1}, 2980 mAh mL^{-1}) as well as high earth abundance (8.23 wt %) and is inherently safe.[4] Furthermore, the mature mining, refinement, and recycling infrastructure for aluminum metal, coupled with its earth abundance, render aluminum metal low cost and easily adapted to scale.[5−8] Despite the opportunity represented by rechargeable aluminum metal batteries, there are fundamental challenges that have hindered their technological development. Few electrolytes are capable of electroplating and stripping aluminum at room temperature, while few positive electrode materials are both electrochemically compatible with these electrolytes. In addition, most intercalation electrodes are unable to accommodate the high-charge-density Al^{3+} cations.

Organic positive electrode materials have garnered recent interest as a result of their inherent tunability, wide availability, and highly sustainable nature.[9,10] Crucially, because of the fundamental chemical flexibility afforded by adding, removing, and altering functional groups, they can be modified to enhance chemical and electrochemical stability for specific electrolytes as well as to enhance their electrochemical performance, while

Received: June 20, 2022
Revised: August 3, 2022
Published: August 16, 2022

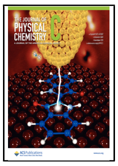

https://doi.org/10.1021/acs.jpcc.2c04272

minimizing dead mass.[11−14] Additionally, organic electrodes contain weak intermolecular bonds (van der Waals and $\pi-\pi$ interactions) that enable fast transport of ions through the organic lattice, a property especially desired for multivalent-ion battery chemistries that hold the promise of higher volumetric charge densities than monovalent ions. Multivalent ion−organic batteries have been previously explored for divalent cations[15] such as magnesium (Mg),[16−19] zinc (Zn),[20,21] and even calcium (Ca).[17,22]

Thus far, there have been a small number of studies on organic positive electrodes with aluminum (Al) metal,[23−34] with a focus on quinone-based molecules, though the nature of the electroactive ions is still poorly understood. Kim et al. performed the first investigation of discrete organic molecules for Al batteries using an organic phenanthrene quinone (PQ) macrocycle where they proposed monovalent $AlCl_2^+$ as the electroactive ion via a combination of time-of-flight secondary ion mass spectrometry (TOF-SIMS) and energy-dispersive X-ray (EDX) spectroscopy.[23] Concordantly, Yoo and Choi put forward $AlCl_2^+$ as the likely electroactive ion for PQ electrodes.[27] In a later study, they introduced a tetradiketone (TDK) molecule that bears an equivalent active site to PQ but within a less aromatic molecule; consequently, they identify divalent $AlCl^{2+}$ to be the preferred electroactive ion to better stabilize reduced TDK.[32] Bitenc et al. probed the active site of 9,10-anthraquinone (AQ) through *operando* FTIR spectroscopy to show the reversible appearance and disappearance of C═O and C−O vibrations, respectively.[24] In subsequent studies on AQ, the Johansson group proposes $AlCl^{2+}$ as the electroactive ion via X-ray photoelectron spectroscopy (XPS) and EDX spectroscopy.[24,28] Note that AQ has a different active site from the TDK and PQ active sites. More recently, Zhou et al. proposed an alternative charge storage mechanism for AQ suggesting Al^{3+} insertion,[30] which is in opposition to the insertion of polyatomic aluminum cations suggested by previous studies.[24,28] However, there has not yet been an unequivocal, experimental determination of the ionic charge storage mechanisms in quinone-based organic electrodes for aluminum batteries that details both the electroactive ions and active sites.

Here, we introduce indanthrone quinone (INDQ, also known as indanthrone) electrodes for the first time in Al−organic batteries and elucidate experimentally the ionic charge storage mechanism, up from the atomic length scale. Like all vat dyes, INDQ can be reversibly oxidized and reduced.[35] INDQ was chosen as a model compound for its insolubility, redox activity, and nitrogen heteroatoms, which have been shown in lithium batteries to increase cell potential.[12,25] We couple multidimensional, solid-state NMR spectroscopy with electrochemical methods, revealing the tetrahedral nature of INDQ-bound chloroaluminous $AlCl_2^+$ species, the reversible electrochemical enolization mechanism at the INDQ active sites, and the associated structural changes. These findings are generalizable to other anthraquinone-based organic electrodes in aluminum battery systems. Furthermore, we demonstrate a powerful solid-state NMR methodology composed of dipolar-mediated correlations and filters to establish molecular-level host−guest interactions while removing undesired signals from mobile electrolyte species.

■ METHODS

Composite Electrode Preparation. Composite electrodes were prepared by ball-milling INDQ (65 wt %; TCI, >97.0%) with carbon black (25 wt %; Super-P, Alfa Aesar, 99%) for 1 h. Poly(vinylidene fluoride) (PVDF) binder (Sigma-Aldrich, average molecular weight of 534000 g/mol) was dissolved in *N*-methyl-2-pyrrolidone (NMP) to form a 5 wt % solution. The PVDF solution was added to the INDQ/Super-P mixture, resulting in a INDQ:Super-P:PVDF mass ratio of 65:25:10, which was mixed at 2000 rpm for 10 min with a Thinky Corporation ARE-310 planetary mixer to form an electrode slurry. The slurry was either cast onto molybdenum foil (0.025 mm; Alfa Aesar, 99.95%) or carbon paper (Fuel Cell Store). For solid-state NMR, XRD, and EDX measurements, molybdenum was used as the current collector for ease of electrode harvesting, while carbon paper was used for all electrochemical measurements. The composite INDQ electrode was dried overnight in a fume hood and subsequently transferred to a vacuum oven at 120 °C for 24 h to evaporate the NMP solvent. The final electrode mass loadings were ∼1 mg cm^{-2}.

Cell Assembly. Cells were assembled inside an argon-filled VAC glovebox with H_2O and O_2 levels below 1 ppm. Poly(tetrafluoroethylene) (PTFE) Swagelok unions of both 0.25 in. (6.35 mm) and 0.50 in. (12.70 mm) diameters were used as the cell bodies, with molybdenum rods as current collectors for both electrodes, and sealed to be airtight. A glass microfiber filter (GF/D, Whatman) was used as the separator material. Aluminum foil (Alfa Aesar, 99.99%, 0.1 mm thickness) was used as the anode material. A Lewis acidic mixture of aluminum chloride (Alfa Aesar; 99.99% metals basis) and 1-ethyl-3-methylimidazolium chloride (Aldrich; ≥98.0%). ([$AlCl_3$:EMIm]Cl) electrolyte was prepared in-house with a molar ratio of 1:1.5. We used 50 and 150 μL of electrolyte for the 0.25 and 0.50 in. diameter cells, respectively. For the cyclic voltammetry tests, three-electrode PTFE T-joint Swagelok cells were used with an aluminum wire as a quasi-reference.

Electrochemical Measurements. Galvanostatic cycling experiments were performed on an Arbin Instruments LBT battery cycler using lower and upper voltage limits of 0.2 and 2.25 V, respectively. Cyclic voltammetry measurements were performed on a six-channel BioLogic VSP-300 potentiostat in various ranges, with a maximum of 0.05−2.45 V corresponding to the working window of the electrolyte. The open-circuit potential (OCP) for the Al-INDQ cells is typically ca. 1.75 V immediately after construction. After cycling, the OCP is generally ca. 1.3 V.

Electrode Harvesting. Following electrochemical measurements, cells were disassembled in an argon-filled glovebox. Organic electrodes were removed from the cell bodies and blotted dry to remove excess electrolyte from the electrode surface. For solid-state NMR measurements the electrode was then removed from the Mo foil current collector and packed into a 1.6 mm zirconia rotor.

X-ray Diffraction (XRD). XRD measurements were performed by using a PANalytical X'Pert Pro powder diffractometer with a Cu Kα radiation source (λ = 0.544 nm). A scan rate of 0.2° min^{-1} was used to scan a 2θ range of 7.5°−45°.

Energy-Dispersive X-ray Spectroscopy. Energy-dispersive X-ray spectroscopy was performed by using a Zeiss Supra 55 field emission scanning electron microscope under high vacuum.

Density Functional Theory (DFT). DFT calculations were performed by using Gaussian 09.[36] The molecular geometry was optimized by using the 6-31G(d,p) basis set and the hybrid B3LYP method (Becke's three-parameter nonlocal exchange functional and Lee−Yang−Parr's correlation functional). The INDQ structure was first optimized. Then, four $AlCl_2^+$

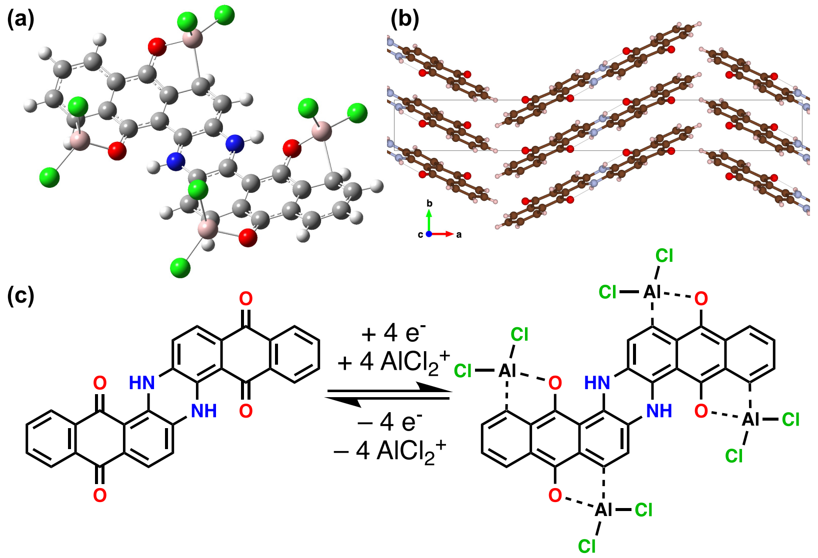

Figure 1. (a) DFT-calculated structure of INDQ with four complexed $AlCl_2^+$ cations.[36] (b) Crystal structure of pristine INDQ.[46,47] (c) Proposed electrochemical reaction scheme of INDQ in Lewis acidic $AlCl_3$:[EMIm]Cl electrolyte. Atoms in (a) are colored as follows: Cl = green, Al = pink, O = red, N = blue, C = gray, and H = white.

molecules were added and assigned a 1+ charge (total 4+), while the INDQ structure was assigned a 4− charge. The structure was subsequently relaxed to determine the most energetically favorable configuration.

Nuclear Magnetic Resonance (NMR) Spectroscopy. Solid-state NMR spectra were acquired on a Bruker AVANCE III HD 600 NMR spectrometer with a 14.1 T narrow-bore superconducting magnet operating at 600.140 MHz for ^1H, 156.378 MHz for ^{27}Al, and 150.910 MHz for ^{13}C. A Phoenix NMR 1.6 mm HXY magic-angle-spinning (MAS) probehead was used, where all measurements were conducted by using MAS rates of 40 kHz. To mitigate MAS-induced sample heating, air at a temperature 293.2 K was pumped through the probehead at 600 L h^{-1}. ^1H and ^{13}C shifts were referenced with respect to tetramethylsilane (TMS) at 0 ppm by using adamantane as a secondary chemical shift reference. ^{27}Al shifts were referenced to 1 M aqueous $Al(NO_3)_3$ at 0 ppm.

Solid-state ^{27}Al single-pulse MAS NMR experiments were acquired calibrated to be quantitative by using (i) a recycle delay (0.25 s) such that all nuclear spins relax to thermal equilibrium between pulses ($>5 \times T_1$ of ^{27}Al), where T_1 is the longitudinal relaxation time) and (ii) short $\pi/12$ radio-frequency (rf) pulses to ensure uniform excitation of all quadrupolar ^{27}Al nuclear spins (spin = 5/2) within a linear regime.[37,38] Here, all quantitative solid-state ^{27}Al NMR experiments were performed by using $\pi/12$ pulses of 0.32 μs, which were calculated based on the optimum $\pi/2$ pulse length of 1.9 μs (rf field strength ν_1 of 132 kHz) for 1 M aqueous $Al(NO_3)_3$.

One- and two-dimensional $^{27}Al\{^1H\}$ dipolar-mediated heteronuclear multiple quantum correlation ($^{27}Al\{^1H\}$ D-HMQC) experiments were used to establish $^{27}Al-^1H$ molecular proximities and filter mobile ^{27}Al signals from excess electrolyte. The symmetry-based $SR4_1^2$ recoupling pulse scheme was used to recouple $^{27}Al-^1H$ dipolar interactions, which also simultaneously decouples $^1H-^1H$ interactions.[39,40] ^{27}Al central-transition-selective $\pi/2$ and π pulses of 12 and 24 μs were used, respectively. The ^1H rf field of 80 kHz (2 × MAS rate) was used for the $SR4_1^2$ pulses. For ^{27}Al signal enhancement, a preparatory 21 kHz strength ^{27}Al double-frequency sweep (DFS) pulse starting from an offset of 1 MHz to 100 kHz was applied for 750 μs prior to each scan.[41,42]

All solid-state ^1H broadband rf pulses had an rf field strength of 161 kHz ($\pi/2$ pulse of 1.55 μs). The ^1H spin-echo MAS experiments were acquired by using an echo delay of one rotor period (25 μs) between the $\pi/2$ and π pulses and a recycle delay of 3 s ($>5 \times T_1$ of ^1H). ^1H spin-echo instead of single-pulse MAS experiments were used to minimize probe background signal. The ^1H spin-echo experiments yielded quantitative signal intensities because the total echo delay of two rotor periods (50 μs) was much smaller than the transverse ^1H T_2 relaxation times. To remove mobile ^1H signals from excess electrolyte, $^1H\{^1H\}$ dipolar-mediated double-quantum-filtered (D-DQF) spectra were acquired by using the BaBa-xy8 pulse sequence.[43]

To enhance signal sensitivity, $^{13}C\{^1H\}$ cross-polarization magic-angle-spinning (CP-MAS) experiments were used to characterize ^{13}C nuclei. The $^{13}C\{^1H\}$ CP-MAS experiment uses spin-locking pulses on ^{13}C and ^1H with rf fields that satisfy the Hartmann−Hahn matching condition.[44,45] During cross-polarization, ^1H and ^{13}C rf field strengths of 100 and 20 kHz were used, respectively (zero-quantum $n = +2$ condition). $^{13}C\{^1H\}$ CP-MAS contact times of 4 ms were used unless otherwise specified.

■ RESULTS AND DISCUSSION

DFT Calculations of $AlCl_2^+$ Binding. Quantum chemical calculations of chloroaluminous ($AlCl_2^+$) ions with an indanthrone quinone (INDQ) molecule indicate that $AlCl_2^+$ cations complex with the oxygen atoms of INDQ. The calculations showed two sets of symmetrical binding environments per INDQ molecule for a total of four binding sites, localized at the reduced C═O moiety (Figure 1a). Assuming a one-electron reduction reaction per carbonyl group in the molecule (i.e., a four-electron reduction per INDQ molecule), the theoretical capacity of INDQ is 242 mAh g^{-1}. The carbonyl groups undergo electrochemical enolization to form negatively charged C−O groups. DFT calculations show the complexed $AlCl_2^+$ species additionally coordinate to a nearby carbon atom which results in a tetrahedrally coordinated aluminum atom that

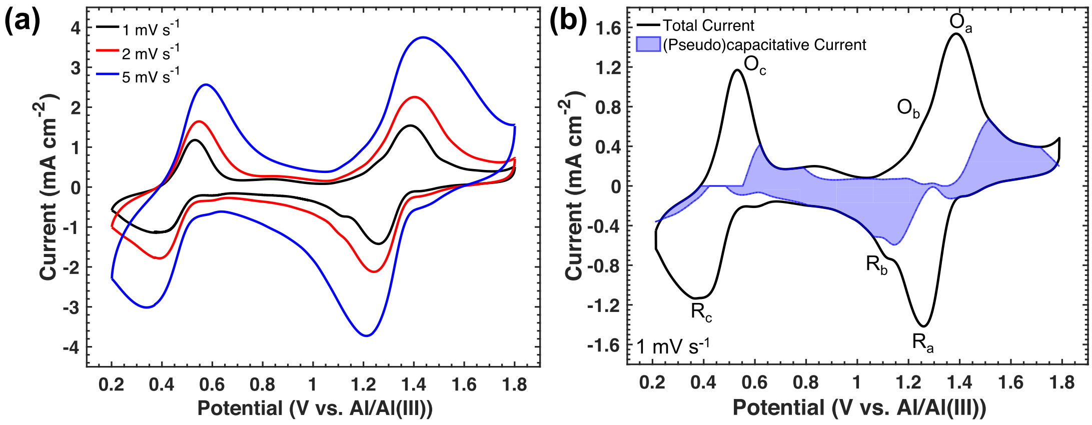

Figure 2. Electrochemical characterization of Al-INDQ three-electrode cells. (a) Variable-rate cyclic voltammetry at 1, 2, and 5 mV s^{-1} rates with a potential range of 0.2−1.8 V. (b) Current deconvolution on a 1 mV s^{-1} cylic voltammogram showing (pseudo)capacitive contributions to the current (blue shaded area).

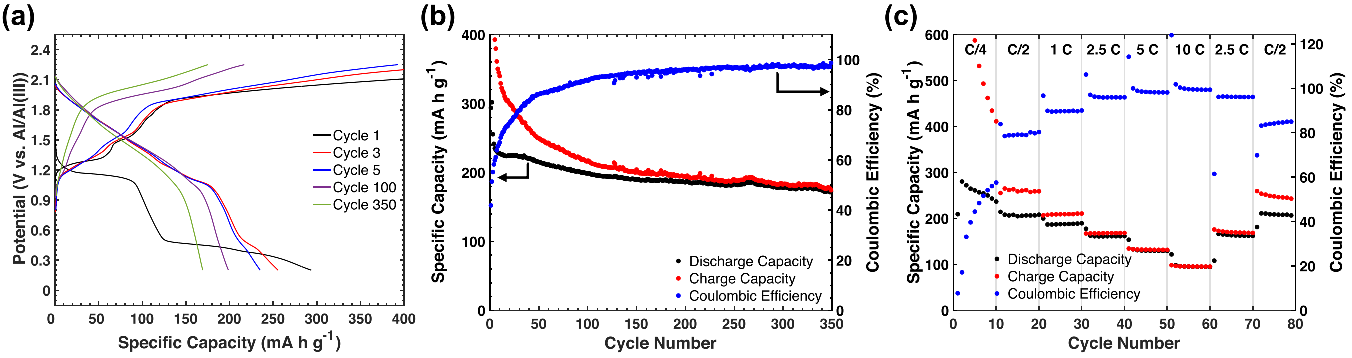

Figure 3. Galvanostatic cycling of Al-INDQ cells. (a) Galvanostatic cycling curves at 100 mA g^{-1} (C/2.4) cycling rate. (b) Long-term galvanostatic cycling statistics at 100 mA g^{-1} (C/2.4) cycling rate. (c) Variable-rate galvanostatic cycling with rates between C/4 and 10 C (1 C = 240 mAh g^{-1}). The specific capacity axis in (a) was shortened for clarity; the full axis can be found in Figure S3a.

is supported experimentally by solid-state ^{27}Al NMR measurements below. Note that $AlCl_2^+$ binding to carbonyl active sites is corroborated by previous literature on Al-organic batteries.[23,24,27] The crystal structure of pristine INDQ, solved by Bailey,[46] reveals that INDQ molecules stack into planar sheets (Figure 1b). These planar stacks may also enable $AlCl_2^+$ to bind tetrahedrally between INDQ molecules in adjacent layers; however, this is not expected to be the dominant case due to consistently achieved discharge capacities close to the theoretical capacity at low rates. The overall reaction scheme is presented in Figure 1c.

Electrochemical Characterization of Al-INDQ Cells. Variable-rate cyclic voltammetry (CV) of INDQ in a three-electrode cell was performed to electrochemically characterize the nature of the electrochemical reactions occurring (Figure 2a). The voltammograms exhibit three major sets of quasi-reversible, Faradaic reactions, labeled *a*, *b*, and *c*, where R and O represent reduction and oxidation, respectively (Figure 2b). We expect only two sets of reversible redox peaks with similar potentials, corresponding to electrochemical enolization of the two distinct but chemically similar carbonyl groups present on INDQ, resulting in reduction potentials at ca. 1.25 V (R_a) and 1.15 V (R_b). The discharge potentials of E_a and E_b show a modest improvement compared to that of anthraquinone (1.1 V),[24] likely a result of the nitrogen heteroatoms in the structure.[11,12,26]

The nature of the reaction at 0.4 V (R_c) is unclear but is possibly a result of EMIm$^+$ cations in the ionic liquid electrochemically degrading. EMIm$^+$ has been shown by Hope et al.[48] to decompose via loss of its “carbene” proton, which could be the source of the solid EMIm-like signals observed in the solid-state ^{1}H NMR below. In addition, solid-state ^{27}Al NMR investigations of INDQ electrodes harvested at 0.9 and 0.2 V on the first discharge reveal little difference before and after this reaction, indicating that aluminum does not play a role in R_c. A second reduction plateau for Al−anthraquinone batteries was observed by Bitenc et al.[24] when electrodes are not well wetted before cycling, and similarly by Voskian and Hatton[49] for electrochemical CO_2 complexation by anthraquinone via the same electrochemical reaction scheme under low mass flux of CO_2. In both examples, the second reduction reaction appeared with approximately a 0.2 V difference from the optimized case; because R_c occurs ca. 0.8 V below the electrochemical enolization reactions, these reasons are not expected to be the cause for the lower potential reduction reaction.

The variable-rate cyclic voltammograms (Figure 2a) were analyzed to better understand the generation of the electroactive ion $AlCl_2^+$, which is not native to the electrolyte.[50,51] The cyclic voltammogram at 1 mV s^{-1} (Figure 2b) was disentangled into Faradaic, diffusion-limited contributions to the current as well as non-diffusion-limited current contributions associated with capacitive and pseudocapacitive charge storage. This deconvolution was performed according to the method described in Text S1 (Supporting Information), first described by Wang et al.[52] and comprehensively discussed by Schoetz et al.[53] The Faradaic

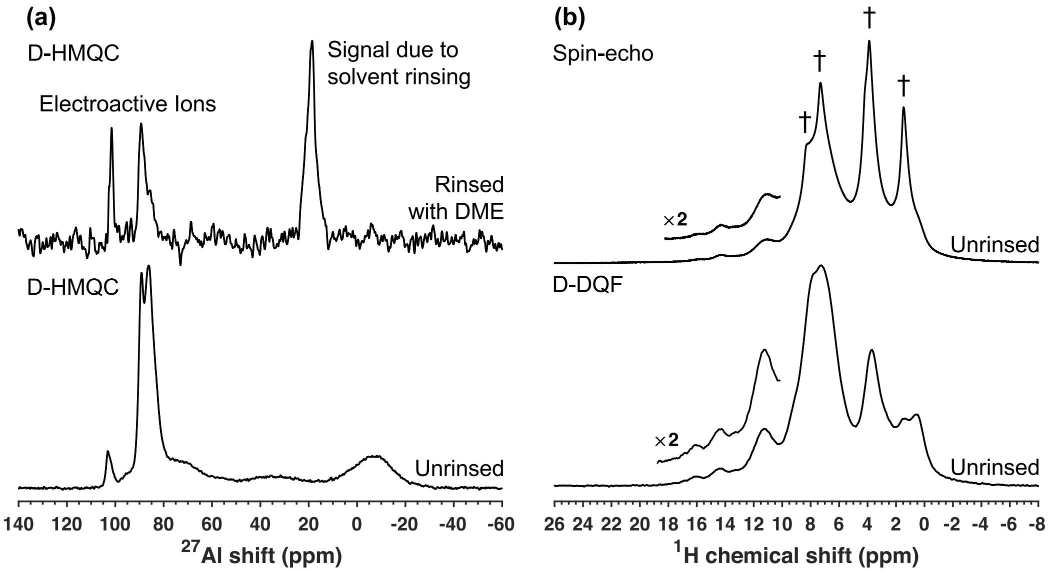

Figure 4. (a) Solid-state $^{27}Al\{^{1}H\}$ D-HMQC NMR spectra of discharged INDQ electrodes (10 mA g^{-1}, cycle 5): rinsed with 1,2-dimethoxyethane (top) as well as unrinsed containing residual electrolyte (bottom). (b) Solid-state ^{1}H spin-echo (top) and $^{1}H\{^{1}H\}$ D-DQF (bottom) NMR spectra of discharged INDQ electrodes (10 mA g^{-1}, cycle 5), both unrinsed containing residual electrolyte. The quantitative ^{1}H spin-echo spectrum reveals all environments in the sample, including both solid INDQ protons and liquid $EMIm^{+}$ cations in the electrolyte (marked with daggers), whereas the $^{1}H\{^{1}H\}$ D-DQF spectrum filters out the mobile $EMIm^{+}$ ^{1}H signals.

contribution to the current was determined to be 63% within the potential window 0.2−1.8 V. The deconvolution also highlighted that the Faradaic, diffusion-limited electrochemical enolization reactions are each followed by a region of non-diffusion-limited current (Figure 2b, blue shaded region) that is commensurate with the proposed generation of charge-compensating cations at the electrode surface that subsequently coordinate to INDQ via the reaction scheme:

$$2Al_2Cl_7^{-} \rightleftarrows AlCl_2^{+} + 3AlCl_4^{-} \qquad (1)$$

The accumulation of these $AlCl_4^{-}$ anions generated at the electrode surface is likely the root cause of the observed (pseudo)capacitance. The proposed reaction scheme is further validated by the solid-state NMR analyses discussed in detail in the subsequent sections.

Electrochemical performance was tested through galvanostatic cycling of Al-INDQ cells. Cells were cycled to an upper cutoff potential of 2.25 V to ensure completeness of reaction while accounting for overpotentials experienced at higher rates. The capacitive current following the electrochemical enolization reactions can extend hundreds of millivolts beyond the Faradaic reactions (Figure S1, Supporting Information). The galvanostatic cycling curves at 100 mA g^{-1} (Figure 3a) highlight changes occurring over the initial cycles, with minimal change in the discharge profiles from cycle 3 to cycle 350. There is, however, a pronounced difference between the initial discharge and those of subsequent cycles. We hypothesize that this change is the result of two effects. First, disorder is imparted when $AlCl_2^{+}$ cations first electrochemically complex with pristine INDQ, as measured by XRD (Figure S2) and solid-state $^{13}C\{^{1}H\}$ HETCOR NMR measurements (discussed below), which broadens the galvanostatic discharge plateaus after the first cycle. Second, the electrochemical intercalation of $AlCl_4^{-}$ anions may occur between the conjugated $\pi-\pi$ stacked ring systems in INDQ upon charge. A similar phenomenon was studied by Kong et al. investigating various polyaromatic hydrocarbons including anthracene, an analogue of anthraquinone without a specific active site, where they observed charging between 1.5 and 2.3 V with corresponding discharge potentials between 1 and 2 V.[34]

The corresponding plot of capacities and Coulombic efficiencies as a function of cycle number (Figure 3b) demonstrate specific capacities approaching 200 mAh g^{-1} for several hundred cycles, a value close to the theoretical capacity of 242 mAh g^{-1}. A loss of capacity over the initial few cycles appears to be a common trend with many organic battery systems studied so far,[11,23−26,54] which appears to be most common with smaller, less rigid molecules that are more liable to dissolve including in their partially charged forms, as observed in organic electrodes for Mg-ion batteries.[16] The charge capacity decreases over the first 100 cycles or so, approaching the value of the discharge capacity (Figure 3b).

Galvanostatic cycling was performed at different current densities to assess the electrochemical rate performance of INDQ electrodes. Variable-rate galvanostatic cycling reveals that at rates up to 2400 mA g^{-1} (10 C rate) cells still achieved over 100 mA hg^{-1} (Figure 3c). We hypothesize that Al-INDQ cells are capable of such fast rate performance due to (i) the reduced desolvation penalty to form electroactive $AlCl_2^{+}$ cations from $Al_2Cl_7^{-}$ anions (eq 1), compared to trivalent Al^{3+};[26] (ii) the significantly lower free energy of solvation for the ions within the chloroaluminate ionic liquid electrolyte, compared to organic carbonate-based electrolytes;[55] (iii) the monovalent nature of both the electroactive $AlCl_2^{+}$ cation and $Al_2Cl_7^{-}$ anion, which exhibit faster mass transfer and electrochemical kinetics compared to multivalent counterparts (e.g., Al^{3+}); and (iv) the lack of a solid electrolyte interphase (SEI) layer, which would add a significant mass transfer resistance. Note also that the Coulombic efficiency improves as the rate increases. For example, the Coulombic efficiency was 89.7% at 240 mA g^{-1} (1 C) and 99.5% at 2400 mA g^{-1} (10 C). This improvement is due to the kinetic suppression of electrolyte side reactions,[56] as previously observed in Al−graphite batteries.[57]

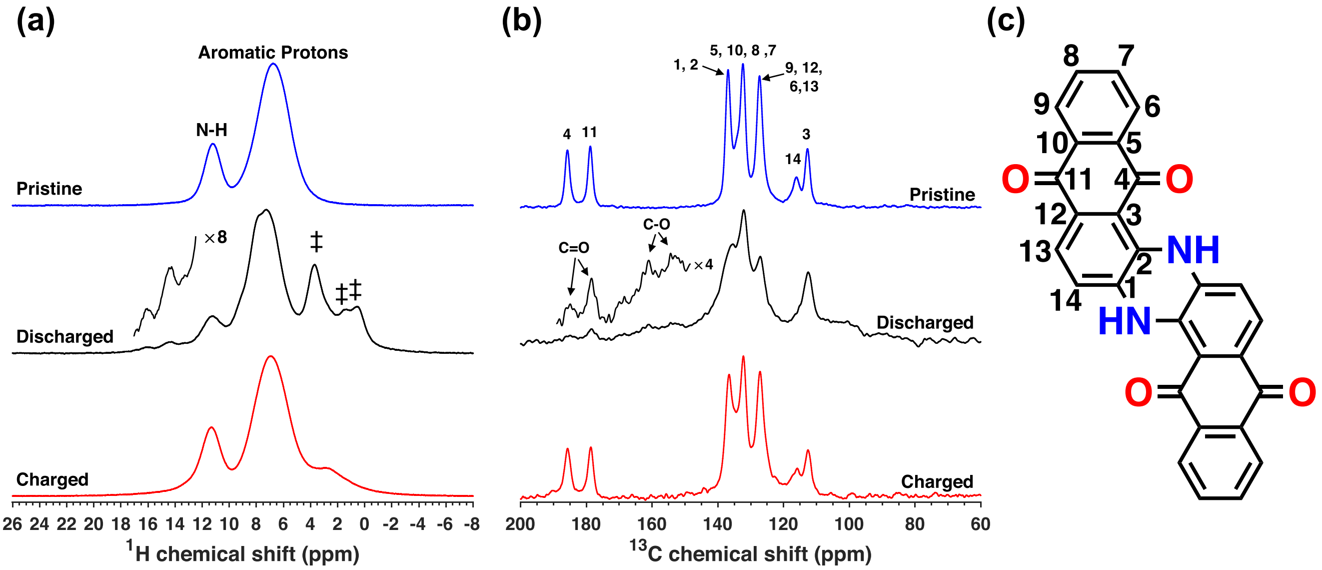

Figure 5. (a) $^{1}H\{^{1}H\}$ D-DQF NMR spectra of pristine INDQ electrodes as well as discharged (10 mA g^{-1}, cycle 5) and charged (10 mA g^{-1}, cycle 3) electrodes. Signals due to solid electrolyte-decomposition products are indicated with double daggers. (b) $^{13}C\{^{1}H\}$ CP-MAS spectra of pristine INDQ as well as discharged and charged electrodes highlighting the electrochemical enolization through the loss of C=O signals. ^{13}C signal assignments are given over the INDQ structure. (c) Structure of pristine INDQ.

Surface Characterization of Cycled INDQ Electrodes. Chlorine/aluminum ratios on discharged INDQ electrode surfaces were determined via EDX analysis. The elemental analysis returned a Cl/Al ratio of ca. 1.84, found by averaging the atomic ratios of 15 different locations on a discharged INDQ electrode, a finding consistent with other Al−quinone studies,[23,27] which suggests the electroactive ion is $AlCl_2^+$. It is possible that there is some quantity of divalent $AlCl^{2+}$ present that would skew the ratio down from 2.00 (for stoichiometric $AlCl_2^+$). This deviation may also be due to decomposition of the electroactive ions in air, as the EDX analysis of the same sample after 2 weeks in ambient conditions yielded a lower Cl/Al ratio of 1.25. This aluminum decomposition product is observed in NMR and is further addressed below.

Chemical and Structural Changes Up from the Atomic Scale. To investigate how INDQ changes upon electrochemical cycling up from the atomic scale, quantitative single-pulse and dipolar-mediated solid-state NMR techniques were employed at different states of charge. Note that solution-state NMR characterization was not possible; INDQ was selected, in part, for its low solubility in many solvents. Solid-state dipolar-mediated NMR experiments leverage the through-space magnetic dipole−dipole interactions between nuclei, which depend upon internuclear distances and molecular mobilities. Dipolar-mediated experiments typically probe subnanometer-scale distances to establish through-space internuclear interactions between nonmobile species. Three types of dipolar-mediated NMR experiments were used in this study: $^{13}C\{^{1}H\}$ CP-MAS, $^{27}Al\{^{1}H\}$ D-HMQC, and $^{1}H\{^{1}H\}$ D-DQF. Further details on dipolar-mediated NMR experiments are given in Text S2, and pulse program schematics are shown in Figure S4. Crucially, solid-state dipolar-mediated NMR experiments enable the composite INDQ electrodes to be characterized without solvent rinsing, as they filter out signals from mobile species in the residual liquid electrolyte. Solvent rinsing was discovered to generate additional aluminum environments, which could be misinterpreted as electroactive ions, as shown in the comparison of $^{27}Al\{^{1}H\}$ D-HMQC spectra acquired on rinsed and unrinsed discharged INDQ electrodes (Figure 4a). Similarly, in the unrinsed electrode, the ^{1}H spin-echo experiment reveals multiple ^{1}H signals associated with $EMIm^+$ cations in the electrolyte, which are filtered by the $^{1}H\{^{1}H\}$ D-DQF experiment (Figure 4b).

The $^{1}H\{^{1}H\}$ D-DQF spectra for pristine, discharged, and charged INDQ electrodes (Figure 5a) reveal the appearance of strongly H-bonded protons upon discharge, which is reversible upon charge. The pristine spectrum contains two regions: an N−H ^{1}H signal at 11.2 ppm and a broad aromatic ^{1}H signal containing multiple environments centered at 6.8 ppm. The aromatic protons in the discharged spectrum also occur over a broad range but have two discernible ^{1}H signals at 7.3 and 7.8 ppm. Emergent ^{1}H signals at 14.4 and 16.0 ppm observed in the discharged sample are due to strongly hydrogen-bonded N−H protons, a result of increased electron density on the nearby reduced oxygen. The ^{1}H signals at 3.7, 1.4, and 0.5 ppm (double daggers, Figure 5a) are likely associated with solid electrolyte decomposition products. The ^{1}H signal at 3.7 ppm is associated with an aluminum decomposition product, as shown below.

Solid-state $^{13}C\{^{1}H\}$ CP-MAS experiments were performed at different states of charge (Figure 5b) to characterize changes in the INDQ carbon framework environments, yielding molecular insights into the nature of the electrochemical redox reactions. Notably, the spectrum of the pristine INDQ exhibits two ^{13}C signals at 178.8 and 185.6 ppm (carbons "4" and "11", Figure 5c) associated with the two distinct carbonyl moieties in INDQ. Upon discharge, these two ^{13}C carbonyl signals are greatly diminished while two new signals are observed at 154.5 and 161.4 ppm, which are assigned to C−O environments, consistent with ^{13}C assignments for similar ^{13}C environments.[58] The C−O signal intensities are weak, which may be a result of paramagnetic relaxation effects from radicals belonging to partly reduced semiquinone species. As suggested in previous literature,[23,24,27] this C−O group is expected to be the binding site for quinone-type molecules. Upon charging, the $^{13}C\{^{1}H\}$ CP-MAS spectrum closely resembles that of the pristine molecule, indicating high reversibility at the molecular level.

Assignments were assisted by the use of varied cross-polarization contact times for both pristine and discharged samples (Figure S5).

To determine changes in long-range periodic atomic ordering after cycling, XRD was performed on INDQ electrodes at different states of charge. (Figure S2). The XRD of the pristine INDQ composite electrode contained reflections from the (001), (400), and (20−1) planes, which disappeared upon cycling, likely due to a distribution of intermolecular spacing introduced by electroactive ions intercalated between the weakly $\pi-\pi$-bonded layers. As discussed previously, this distribution of interlayer spacing could result in the broadening observed in the galvanostatic discharge curves beyond cycle 1. The charged and discharged XRD patterns did not differ greatly from each other, indicating this distribution of intermolecular spacings is an irreversible structural rearrangement in the long-range order in the crystal. However, through solid-state NMR, we show that the electrochemical energy storage reactions are highly reversible at the molecular level.

Molecular-Level Nature of the Electroactive Ions. Solid-state ^{27}Al NMR measurements were performed on discharged and charged INDQ electrodes to understand the aluminum environments present and determine the reversibility of the electrochemical complexation of aluminum (Figure 6a).

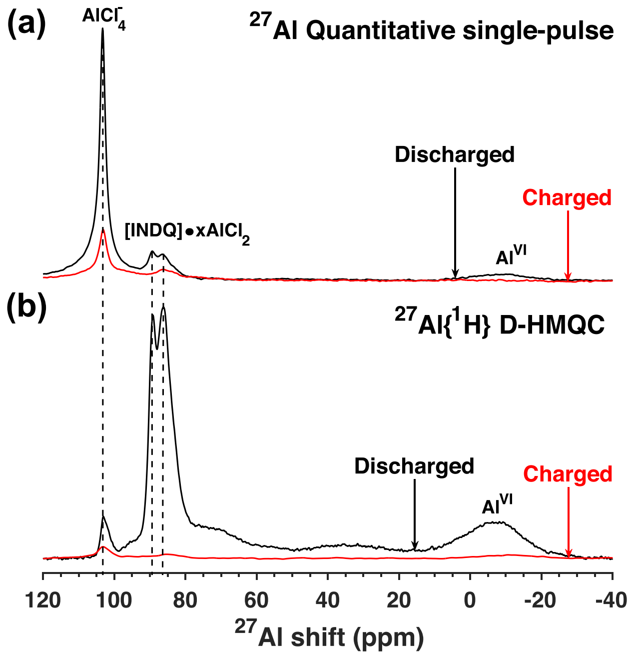

Figure 6. Solid-state ^{27}Al NMR spectra of discharged (black) and charged (red) INDQ electrodes. (a) Solid-state ^{27}Al single-pulse MAS experiments acquired under quantitative conditions. (b) ^{27}Al{^{1}H} D-HMQC experiments with 600 μs recoupling times.

Solid-state ^{27}Al single-pulse measurements acquired under quantitative conditions on the discharged composite electrode yielded multiple distinct aluminum environments: three ^{27}Al signals in the tetrahedral region at 86, 89, and 103 ppm and one weak, broad ^{27}Al signal in the octahedral region at −7 ppm. Aluminum coordination is highly reversible via significant reduction of the tetrahedral ^{27}Al signals upon charge.

As described above and in Text S2, solid-state ^{27}Al{^{1}H} D-HMQC experiments yield signal intensities that depend upon the strength of the heteronuclear ^{27}Al−^{1}H dipolar couplings, which depend upon recoupling times, internuclear distances, and relative mobilities (Figure S6 demonstrates the effect of recoupling time on the ^{27}Al signal observed). In the ^{27}Al{^{1}H} D-HMQC spectrum, the relative intensities of the two tetrahedral aluminum environments at 86 and 89 ppm are significantly greater compared with the quantitative ^{27}Al single-pulse spectrum. These tetrahedrally coordinated aluminum species, which are in close subnanometer-scale proximity to the solid organic material and are mostly absent upon charge, are thus the charge-compensating electroactive ions. Existing studies on Al−quinone batteries suggest the electroactive ions in n-type organic positive electrodes are $AlCl_2^+$ molecular cationic species coordinating to C−O groups.[23,24,27] Previous ^{27}Al NMR studies on tetrahedral, chlorine-ligated aluminum species with organic ligands such as $[AlCl_2(OMe)]_2$, and $[AlCl_2(OEt)]_2$ indicate that $AlCl_2$ moieties coordinated to alkoxy species should fall in the range of ca. 86−97 ppm, with a slightly lower shift for O−Ar coordination.[59−61] To confirm that aluminum coordination primarily occurs following electrochemically driven enolization, ^{27}Al{^{1}H} D-HMQC experiments were also performed on an INDQ electrode that was assembled in a cell but not cycled for 3 days (Figure S7). No INDQ-coordinated ^{27}Al species were observed, verifying the role of these tetrahedral aluminum species as the electroactive ions.

The sharp ^{27}Al signal at 103 ppm in the solid-state quantitative ^{27}Al single-pulse experiment is due to $AlCl_4^-$ from the residual electrolyte. A weak ^{27}Al signal associated with these $AlCl_4^-$ anions persists in the dipolar-mediated ^{27}Al{^{1}H} D-HMQC experiments for both discharged and charged electrodes. This result indicates that there is some $AlCl_4^-$ near the INDQ framework, as evidenced by the existence of heteronuclear ^{27}Al−^{1}H dipolar couplings between the $AlCl_4^-$ and the INDQ protons. When the same ^{27}Al{^{1}H} D-HMQC experiment is repeated without recoupling the dipolar interaction, no $AlCl_4^-$ signal is observed (Figure S8), as expected. In addition, if the species had formed new bonds, the coordination environment would change and the ^{27}Al signal would shift drastically, which is not observed. The octahedral ^{27}Al signal at −7 ppm, which is weak in intensity in the solid-state quantitative ^{27}Al single-pulse spectrum, is likely the six-coordinate electrolyte hydrolysis product observed by Ferrara et al.[50] This species might be formed as a result of minute air ingress into the NMR rotor.

The solid-state ^{13}C{^{1}H} HETCOR experiment of the discharged INDQ electrode (Figure 7a) establishes the through-space interactions between ^{13}C and ^{1}H environments. The 1D ^{13}C and ^{1}H spectra shown along the axes (Figure 7b,c) are identical with those in Figure 5a,b and shown for clarity. In the ^{13}C{^{1}H} HETCOR spectrum there is correlated 2D signal intensity between most ^{13}C signals and the ^{1}H signal at 11.2 ppm associated with N−H protons that exist as a consequence of intermolecular dipolar interactions. Note that the ^{13}C{^{1}H} HETCOR spectrum of INDQ after just one discharge has lower intensity of these intermolecular ^{1}H−^{13}C interactions, indicating further that the intermolecular INDQ spacing plays a role in the shape of the discharge curve. Additionally, there is correlated 2D signal intensity between the aromatic protons and the ^{13}C signal at 154 ppm assigned to C−O moieties, confirming this ^{13}C environment to be part of the main INDQ spin system.

The 2D ^{27}Al{^{1}H} D-HMQC spectrum (Figure 7d) of the discharged INDQ electrode establishes through-space interactions between the ^{27}Al (Figure 7e) and ^{1}H moieties (Figure 7c), further confirming the nature of the electroactive ions at a

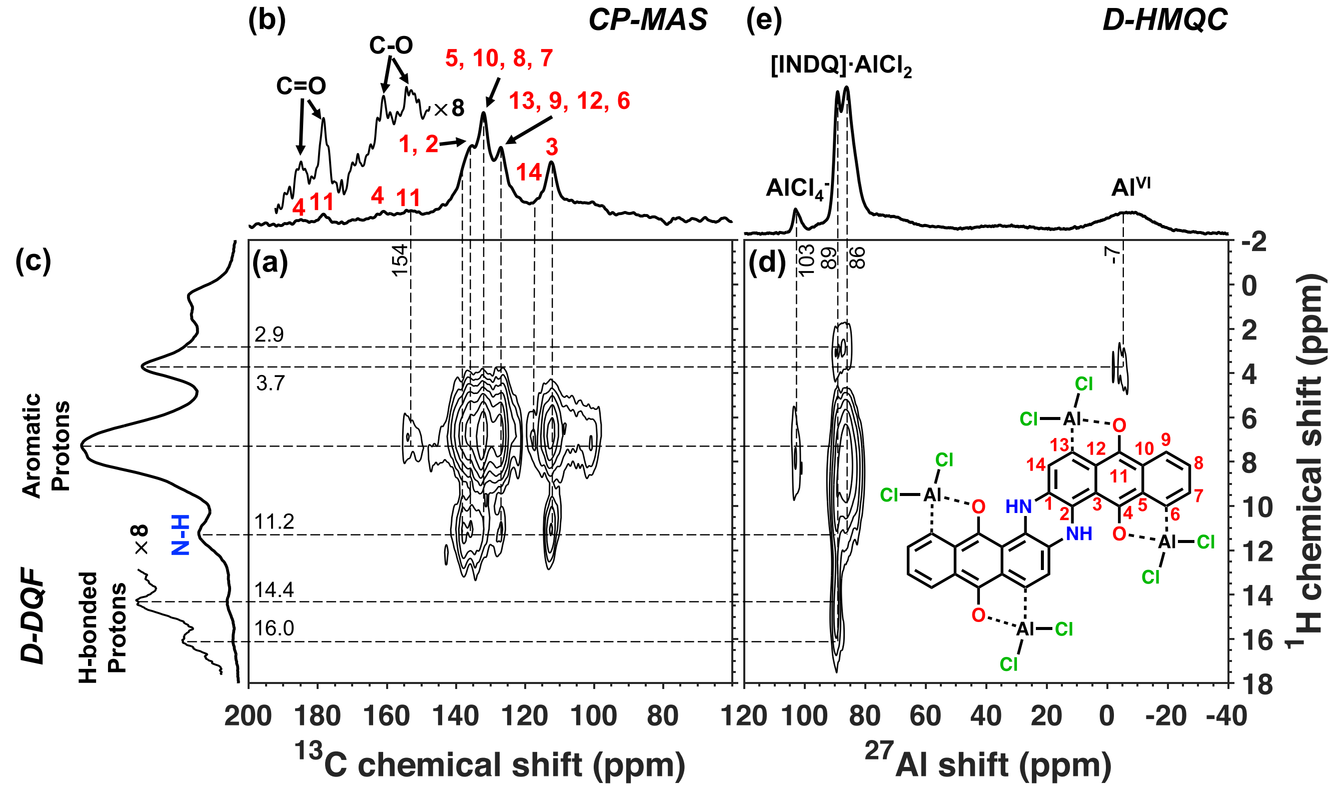

Figure 7. Solid-state 2D dipolar-mediated NMR experiments on an INDQ electrode after galvanostatic discharge (10 mA g^{-1}, cycle 5) acquired at 40 kHz MAS and 14.1 T. (a) 2D ^{27}Al{^{1}H} D-HMQC spectrum with separately acquired (b) ^{27}Al{^{1}H} D-HMQC and (c) ^{1}H{^{1}H} D-DQF spectra. (d) ^{13}C{^{1}H} HETCOR spectrum and separately acquired (e) ^{13}C{^{1}H} CP-MAS. The results establish subnanometer-scale proximities between ^{27}Al and ^{13}C with ^{1}H atoms within the INDQ structure (inset).

molecular level. The 1D ^{27}Al spectrum is identical with the corresponding ^{27}Al{^{1}H} D-HMQC spectrum (Figure 6). The two strong, tetrahedral ^{27}Al environments at 86 and 89 ppm corresponding to $AlCl_2^+$ cations are coupled with the aromatic INDQ protons, indicating that $AlCl_2^+$ is the electroactive ion. These two ^{27}Al environments are also coupled to the new ^{1}H species at 2.9 ppm, indicating that this ^{1}H signal corresponds to an INDQ proton environment not present in the pristine and charged electrodes. The two coordinated tetrahedral aluminum species can be further distinguished from each other. The ^{27}Al environment at 89 ppm is strongly correlated to the emergent hydrogen-bonded ^{1}H environments at 14.4 and 16.0 ppm and is more strongly correlated to the ^{1}H signal at 11.2 ppm (N−H) compared to the ^{27}Al environment at 86 ppm. These stronger interactions indicate that the $AlCl_2^+$ ^{27}Al species at 89 ppm interacts with the C−O group at carbon “4”. In addition, as evident from the 1D ^{27}Al{^{1}H} D-HMQC experiment (Figure 6b), there are ^{1}H−^{27}Al interactions between $AlCl_4^-$ and INDQ protons, likely a result of the generation of $AlCl_2^+$ at the electrode surface, as proposed by eq 1. Lastly, the correlation between the octahedral ^{27}Al species at −7 ppm and the ^{1}H signal at 3.7 ppm indicate that this species is a side reaction product between residual electrolyte and air.

Similar 2D solid-state dipolar-mediated NMR spectra acquired on a charged INDQ electrode (Figure 8) highlight the key differences in both ^{1}H−^{13}C correlations and ^{1}H−^{27}Al correlations. In the ^{13}C{^{1}H} HETCOR (Figure 8a), many of the signal assignments can be made, such as the 2D correlated signal intensity between the ^{13}C at 186 ppm associated with C=O moieties and the ^{1}H signal at 11.2 ppm due to N−H protons, which confirm the ^{13}C assignment of carbon “4”. Note that the N−H proton in the charged electrode does not contain the intermolecular ^{1}H−^{13}C interactions observed in the discharged electrode. The 2D ^{27}Al{^{1}H} D-HMQC spectrum of the charged INDQ electrode (Figure 8d) maintains weak 2D signal correlations between the tetrahedral ^{27}Al environment at 86 ppm and the aromatic INDQ protons; however, the quantitative ^{27}Al signal intensity is <2% that of the discharged electrode (Figure 6). The ^{27}Al signal due to $AlCl_4^-$ also maintains interactions with aromatic INDQ protons, though quantitatively this ^{27}Al signal is again weaker in intensity (Figure 6).

Electrochemical Charge Storage Mechanism. On the basis of the above electrochemical, spectroscopic, and computational results, we propose the following electrochemical charge storage reaction mechanism for INDQ (Figure 1). INDQ molecules first undergo a symmetric two-electron reduction to produce the diradical anionic semiquinone:

$$[\mathrm{INDQ}] + 2e^- \rightleftarrows [\mathrm{INDQ}]^{2\bullet-} \tag{2}$$

Subsequently, to balance the charge of $INDQ^{2\bullet-}$, $AlCl_2^+$ is generated from $Al_2Cl_7^-$ via complexation, leaving a diradical:

$$[\mathrm{INDQ}]^{2\bullet-} + 4\mathrm{Al_2Cl_7^-} \rightleftarrows [\mathrm{INDQ}]^{2\bullet}\cdot 2\mathrm{AlCl_2} + 6\mathrm{AlCl_4^-} \tag{3}$$

The diradical INDQ undergoes another two-electron reduction, resulting in two full negative charges:

$$[\mathrm{INDQ}]^{2\bullet}\cdot 2\mathrm{AlCl_2} + 2e^- \rightleftarrows [\mathrm{INDQ}]^{2-}\cdot 2\mathrm{AlCl_2} \tag{4}$$

Finally, $AlCl_2^+$ is again generated from $Al_2Cl_7^-$ for charge balancing:

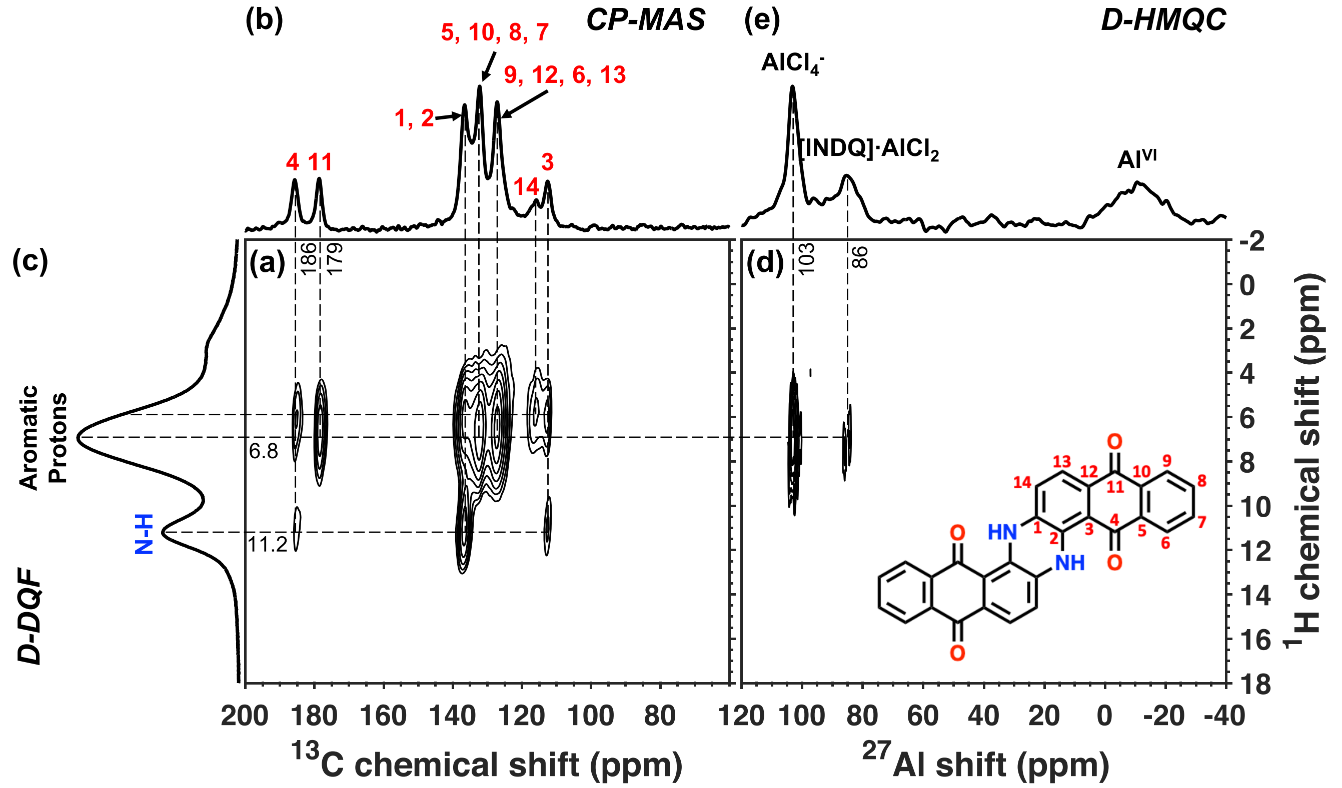

Figure 8. Solid-state 2D dipolar-mediated NMR experiments on an INDQ electrode after galvanostatic charge (10 mA g^{-1}, cycle 3) acquired at 40 kHz and 14.1 T. (a) 2D ^{27}Al{^{1}H} D-HMQC spectrum with separately acquired (b) ^{27}Al{^{1}H} D-HMQC, and (c) ^{1}H{^{1}H} D-DQF spectra. (d) ^{13}C{^{1}H} HETCOR spectrum and separately acquired (e) ^{13}C{^{1}H} CP-MAS. The proton and carbon spectra indicate a return to the pristine structure; additionally, the ^{27}Al spectra intensity is greatly diminished with only weak correlations between the electroactive ion and the electrode.

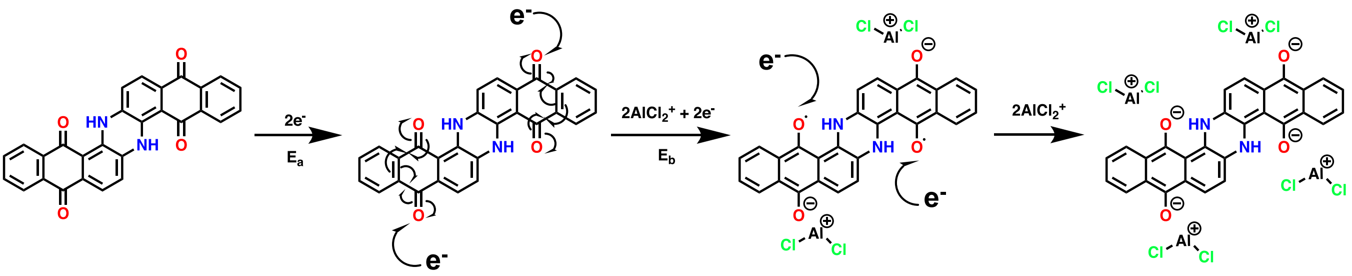

Figure 9. Electrochemical discharge mechanism for INDQ complexation of AlCl$_2^+$, consisting of electrochemical enolization and subsequent charge-balancing steps. Potentials E_a and E_b correspond to reaction potentials defined in the cyclic voltammograms shown in Figure 2.

$$[\mathrm{INDQ}]^{2-}\cdot 2\mathrm{AlCl_2} + 4\mathrm{Al_2Cl_7}^- \rightleftarrows [\mathrm{INDQ}]\cdot 4\mathrm{AlCl_2} + 6\mathrm{AlCl_4}^- \quad (5)$$

The two reduction steps in this case are at almost identical environments, and therefore the reaction potentials are almost equal (E_a and E_b, Figure 2). This reaction scheme is presented in Figure 9.

During discharge, the half-reaction at the INDQ electrode is thus:

$$[\mathrm{INDQ}] + 8\mathrm{Al_2Cl_7}^- + 4e^- \rightleftarrows [\mathrm{INDQ}]\cdot 4\mathrm{AlCl_2} + 12\mathrm{AlCl_4}^- \quad (6)$$

The half-reaction at the aluminum anode is:

$$7\mathrm{AlCl_4}^- + \mathrm{Al} \rightleftarrows 4\mathrm{Al_2Cl_7}^- + 3e^- \quad (7)$$

The overall, balanced full-cell reaction is:

$$3[\mathrm{INDQ}] + 4\mathrm{Al} + 8\mathrm{Al_2Cl_7}^- \rightleftarrows 3([\mathrm{INDQ}]\cdot 4\mathrm{AlCl_2}) + 8\mathrm{AlCl_4}^- \quad (8)$$

We expect the above mechanism to be generalizable to any anthraquinone-based organic electrode material in Lewis acidic chloroaluminate-containing electrolyte. As noted above, however, PQ and TDK are expected to exhibit differences in their charge storage mechanisms as a consequence of the different aromaticities of their active sites.[32]

■ CONCLUSIONS

Indanthrone quinone was introduced as a new positive electrode material for rechargeable aluminum batteries, and for the first time in aluminum−organic batteries, the molecular-level nature of both the organic binding sites and electroactive ions were experimentally elucidated by multidimensional solid-state NMR spectroscopy. Solid-state ^{13}C{^{1}H} CP-MAS NMR spectra conducted at different states of charge showed that INDQ undergoes reversible electrochemical enolization upon cycling. Solid-state ^{27}Al single-pulse and dipolar-mediated NMR experiments revealed aluminum species in tetrahedral coordination environments that were unequivocally complexed with the organic INDQ electrode. The tetrahedral nature of the electroactive ion, in combination with the Cl/Al ratio measured by EDX spectroscopy, establishes $AlCl_2^+$ as the electroactive ion which binds either by concurrent coordination with one oxygen and the aromatic ring system, as predicted by DFT calculations, or intermolecularly between two oxygen atoms of adjacent INDQ molecules. The generation of $AlCl_2^+$ species is consistent with electrochemical analysis that revealed regions of capacitive current following Faradaic enolization reactions. This capacitive current is caused by excess $AlCl_4^-$ produced at the electrode surface, a finding also commensurate with ^{27}Al−^{1}H dipolar interactions observed between $AlCl_4^-$ and INDQ only after electrochemical cycling. In aggregate, these results establish the ionic and electronic charge storage mechanisms of INDQ in chloroaluminate ionic liquid electrolyte, which is expected to be general for other anthraquinone-based organic molecules. This work also highlights solid-state dipolar-mediated NMR methods as powerful tools to study molecular-level changes and interactions in rechargeable metal−organic batteries.

■ ASSOCIATED CONTENT

Supporting Information

The Supporting Information is available free of charge at https://pubs.acs.org/doi/10.1021/acs.jpcc.2c04272.

> An explanation of the current deconvolution of CV; an explanation of dipolar-mediated NMR techniques; variable-rate cyclic voltammograms in a larger electrochemical window with current deconvolution performed; XRD patterns at different states of charge; galvanostatic cycling at a fast rate and with an extended capacity axis; a schematic describing dipolar interaction distances and NMR pulse sequences; NMR spectra showing the effect of varied contact/recoupling times for dipolar-mediated experiments; 1D ^{27}Al{^{1}H} D-HMQC spectra of discharged, charged, and electrolyte soaked INDQ; 1D ^{27}Al{^{1}H} D-HMQC experiments with and without recoupling power (PDF)

■ AUTHOR INFORMATION

Corresponding Author

Robert J. Messinger − *Department of Chemical Engineering, The City College of New York, CUNY, New York, New York 10031, United States; Doctoral Program in Chemistry, The City University of New York, Graduate Center, New York, New York 10016, United States;* orcid.org/0000-0002-5537-3870; Email: rmessinger@ccny.cuny.edu

Authors

Leo W. Gordon − *Department of Chemical Engineering, The City College of New York, CUNY, New York, New York 10031, United States;* orcid.org/0000-0002-8242-9470

Ankur L. Jadhav − *Department of Chemical Engineering, The City College of New York, CUNY, New York, New York 10031, United States*

Mikhail Miroshnikov − *Department of Chemistry & Biochemistry, The City College of New York, CUNY, New York, New York 10031, United States; Doctoral Program in Chemistry, The City University of New York, Graduate Center, New York, New York 10016, United States*

Theresa Schoetz − *Department of Chemical Engineering, The City College of New York, CUNY, New York, New York 10031, United States*

George John − *Department of Chemistry & Biochemistry, The City College of New York, CUNY, New York, New York 10031, United States; Doctoral Program in Chemistry, The City University of New York, Graduate Center, New York, New York 10016, United States;* orcid.org/0000-0002-0382-1256

Complete contact information is available at: https://pubs.acs.org/10.1021/acs.jpcc.2c04272

Notes

The authors declare no competing financial interest.

■ ACKNOWLEDGMENTS

The authors gratefully acknowledge support from the U.S. National Science Foundation (NSF) under CAREER Award CBET-1847552, the U.S. Nuclear Regulatory Commission (NRC) under Award 31310018M0036, and the U.S. National Aeronautics and Space Administration (NASA) via the NASA-CCNY Center for Advanced Batteries for Space under Cooperative Agreement 80NSSC19M0199. DFT calculations were performed at the CUNY High Performance Computing Center at the College of Staten Island, which is supported in part by NSF Awards CNS-0958379, CNS-0855217, and ACI-1126113.

■ REFERENCES

(1) Vikström, H.; Davidsson, S.; Höök, M. Lithium availability and future production outlooks. *Applied Energy* **2013**, *110*, 252−266.

(2) Sonoc, A.; Jeswiet, J. A review of lithium supply and demand and a preliminary investigation of a room temperature method to recycle lithium ion batteries to recover lithium and other materials. *Procedia CIRP* **2014**, *15*, 289−293.

(3) Desai, P.; Nguyen, M. Shortages flagged for EV materials lithium and cobalt. *Reuters Energy* **2021**.

(4) Haynes, W. M.; Lide, D. R.; Bruno, T. J. *CRC Handbook of Chemistry and Physics*, 97th ed.; CRC Press: 2016.

(5) Paraskevas, D.; Kellens, K.; Dewulf, W.; Duflou, J. R. Environmental modelling of aluminium recycling: A Life Cycle Assessment tool for sustainable metal management. *Journal of Cleaner Production* **2015**, *105*, 357−370.

(6) Grimaud, G.; Perry, N.; Laratte, B. Life cycle assessment of aluminium recycling process: case of shredder cables. *Procedia CIRP* **2016**, *48*, 212−218.

(7) Soo, V. K.; Peeters, J.; Paraskevas, D.; Compston, P.; Doolan, M.; Duflou, J. R. Sustainable aluminium recycling of end-of-life products: A joining techniques perspective. *Journal of Cleaner Production* **2018**, *178*, 119−132.

(8) Soo, V. K.; Peeters, J. R.; Compston, P.; Doolan, M.; Duflou, J. R. Economic and environmental evaluation of aluminium recycling based on a belgian case study. *Procedia Manufacturing* **2019**, *33*, 639−646.

(9) Miroshnikov, M.; Kato, K.; Babu, G.; Thangavel, N. K.; Mahankali, K.; Hohenstein, E.; Wang, H.; Satapathy, S.; Divya, K. P.; Asare, H.; Ajayan, P. M.; Arava, L. M. R.; John, G. Made from henna! A fast-charging, high-capacity, and recyclable tetrakislawsone cathode material for lithium ion batteries. *ACS Sustainable Chem. Eng.* **2019**, *7*, 13836−13844.

(10) Deng, Q.; Luo, Z.; Yang, R.; Li, J. Toward organic carbonyl-contained small molecules in rechargeable batteries: a review of current modified strategies. *ACS Sustainable Chem. Eng.* **2020**, *8*, 15445−15465.

(11) Liang, Y.; Zhang, P.; Yang, S.; Tao, Z.; Chen, J. Fused heteroaromatic organic compounds for high-power electrodes of rechargeable lithium batteries. *Adv. Energy Mater.* **2013**, *3*, 600−605.

(12) Shimizu, A.; Tsujii, Y.; Kuramoto, H.; Nokami, T.; Inatomi, Y.; Hojo, N.; Yoshida, J. I. Nitrogen-containing polycyclic quinones as cathode materials for lithiumion batteries with increased voltage. *Energy Technology* **2014**, *2*, 155−158.

(13) Zhang, Y.; Liu, S.; Ji, Y.; Ma, J.; Yu, H. Emerging nonaqueous aluminum-ion batteries: challenges, status, and perspectives. *Adv. Mater.* **2018**, *30*, 1706310.

(14) Miroshnikov, M.; Divya, K. P.; Babu, G.; Meiyazhagan, A.; Arava, L. M. R.; Ajayan, P. M.; John, G. Power from nature: designing green battery materials from electroactive quinone derivatives and organic polymers. *J. Mater. Chem. A* **2016**, *4*, 12370−12386.

(15) Qin, K.; Huang, J.; Holguin, K.; Luo, C. Recent advances in developing organic electrode materials for multivalent rechargeable batteries. *Energy Environ. Sci.* **2020**, *13*, 3950−3992.

(16) Dong, H.; Tutusaus, O.; Liang, Y.; Zhang, Y.; Lebens-Higgins, Z.; Yang, W.; Mohtadi, R.; Yao, Y. High-power Mg batteries enabled by heterogeneous enolization redox chemistry and weakly coordinating electrolytes. *Nature Energy* **2020**, *5*, 1043−1050.

(17) Cang, R.; Zhao, C.; Ye, K.; Yin, J.; Zhu, K.; Yan, J.; Wang, G.; Cao, D. Aqueous calcium-ion battery based on a mesoporous organic anode and a manganite cathode with long cycling performance. *ChemSusChem* **2020**, *13*, 3911−3918.

(18) Bitenc, J.; Pavčnik, T.; Košir, U.; Pirnat, K. Quinone based materials as renewable high energy density cathode materials for rechargeable magnesium batteries. *Materials* **2020**, *13*, 506.

(19) Debashis, T.; Viswanatha, H. M.; Harish, M. N. K.; Sampath, S. Vat orange 11−based organic cathode material for high rate rechargeable magnesium battery. *J. Electrochem. Soc.* **2020**, *167*, 070561.

(20) Zhao, Q.; Huang, W.; Luo, Z.; Liu, L.; Lu, Y.; Li, Y.; Li, L.; Hu, J.; Ma, H.; Chen, J. High-capacity aqueous zinc batteries using sustainable quinone electrodes. *Science Advances* **2018**, *4*, 1−10.

(21) Guo, Z.; Ma, Y.; Dong, X.; Huang, J.; Wang, Y.; Xia, Y. An environmentally friendly and flexible aqueous zinc battery using an organic cathode. *Angew. Chem.* **2018**, *130*, 11911−11915.

(22) Rodríguez-Pérez, I. A.; Yuan, Y.; Bommier, C.; Wang, X.; Ma, L.; Leonard, D. P.; Lerner, M. M.; Carter, R. G.; Wu, T.; Greaney, P. A.; Lu, J.; Ji, X. Mg-ion battery electrode: an organic solid's herringbone structure squeezed upon Mg-ion insertion. *J. Am. Chem. Soc.* **2017**, *139*, 13031−13037.

(23) Kim, D. J.; Yoo, D.-J.; Otley, M. T.; Prokofjevs, A.; Pezzato, C.; Owczarek, M.; Lee, S. J.; Choi, J. W.; Stoddart, J. F. Rechargeable aluminium organic batteries. *Nature Energy* **2019**, *4*, 51−59.

(24) Bitenc, J.; Lindahl, N.; Vizintin, A.; Abdelhamid, M. E.; Dominko, R.; Johansson, P. Concept and electrochemical mechanism of an Al metal anode - organic cathode battery. *Energy Storage Materials* **2020**, *24*, 379−383.

(25) Kao, Y.-T.; Patil, S. B.; An, C.-Y.; Huang, S.-K.; Lin, J.-C.; Lee, T.-S.; Lee, Y.-C.; Chou, H.-L.; Chen, C.-W.; Chang, Y. J.; et al. A quinone-based electrode for high-performance rechargeable aluminum-ion batteries with a low-cost $AlCl_3$/urea ionic liquid electrolyte. *ACS Appl. Mater. Interfaces* **2020**, *12*, 25853−25860.

(26) Guo, F.; Huang, Z.; Wang, M.; Song, W. L.; Lv, A.; Han, X.; Tu, J.; Jiao, S. Active cyano groups to coordinate $AlCl_2^+$ cation for rechargeable aluminum batteries. *Energy Storage Materials* **2020**, *33*, 250−257.

(27) Yoo, D. J.; Choi, J. W. Elucidating the extraordinary rate and cycling performance of phenanthrenequinone in aluminum-complex-ion batteries. *J. Phys. Chem. Lett.* **2020**, *11*, 2384−2392.

(28) Lindahl, N.; Bitenc, J.; Dominko, R.; Johansson, P. Aluminum metal-organic batteries with integrated 3D thin film anodes. *Adv. Funct. Mater.* **2020**, *30*, 3−9.

(29) Yan, L.; Zeng, X.; Zhao, S.; Jiang, W.; Li, Z.; Gao, X.; Liu, T.; Ji, Z.; Ma, T.; Ling, M.; Liang, C.; et al. 9,10-Anthraquinone/$K_2CuFe(CN)_6$: A highly compatible aqueous aluminum-ion full-battery configuration. *ACS Appl. Mater. Interfaces* **2021**, *13*, 8353−8360.

(30) Zhou, L.; Zhang, Z.; Cui, L.; Xiong, F.; An, Q.; Zhou, Z.; Yu, X.-f.; Chu, P. K.; Zhang, K. High-capacity and small-polarization aluminum organic batteries based on sustainable quinone-based cathodes with Al^{3+} insertion. *Cell Rep. Phys. Sci.* **2021**, *2*, 100354.

(31) He, J.; Shi, X.; Wang, C.; Zhang, H.; Liu, X.; Yang, Z.; Lu, X. A quinone electrode with reversible phase conversion for long-life rechargeable aqueous aluminum-metal batteries. *Chem. Commun.* **2021**, *57*, 6931−6934.

(32) Yoo, D. J.; Heeney, M.; Glöcklhofer, F.; Choi, J. W. Tetradiketone macrocycle for divalent aluminium ion batteries. *Nat. Commun.* **2021**, *12*, 1−9.

(33) Wang, G.; Dmitrieva, E.; Kohn, B.; Scheler, U.; Liu, Y.; Tkachova, V.; Yang, L.; Fu, Y.; Ma, J.; Zhang, P. et al. An efficient rechargeable aluminium-amine battery working under quaternization chemistry. *Angewandte Chemie - International Edition.* **2022**, *61*.

(34) Kong, D.; Cai, T.; Fan, H.; Hu, H.; Wang, X.; Cui, Y.; Wang, D.; Wang, Y.; Hu, H. Polycyclic aromatic hydrocarbons as a new class of promising cathode materials for aluminum-ion batteries. *Angewandte Chemie - International Edition* **2022**.

(35) Aspland, J. Vat dyes and their application. *Textile Chemist & Colorist* **1992**, *24*, 22−24.

(36) Frisch, M. J.; Trucks, G. W.; Schlegel, H. B.; Scuseria, G. E.; Robb, M. A.; Cheeseman, J. R.; Scalmani, G.; Barone, V.; Mennucci, B.; Petersson, G. A.; et al. *Gaussian 09*, Revision E.01; Gaussian Inc.: Wallingford, CT, 2009.

(37) Fenzke, D.; Freude, D.; Fröhlich, T.; Haase, J. NMR intensity measurements of half-integer quadrupole nuclei. *Chem. Phys. Lett.* **1984**, *111*, 171−175.

(38) Jadhav, A. L.; Xu, J. H.; Messinger, R. J. Quantitative molecular-level understanding of electrochemical aluminum-ion intercalation into a crystalline battery electrode. *ACS Energy Lett.* **2020**, *5*, 2842−2848.

(39) Levitt, M. H. *Encyclopedia of Magnetic Resonance*; John Wiley & Sons, Ltd.: Chichester, UK, 2007; pp 165−196.

(40) Brinkmann, A.; Kentgens, A. P. Proton-selective ^{17}O-^{1}H distance measurements in fast magic-angle-spinning solid-state NMR spectroscopy for the determination of hydrogen bond lengths. *J. Am. Chem. Soc.* **2006**, *128*, 14758−14759.

(41) Schurko, R. W.; Hung, I.; Widdifield, C. M. Signal enhancement in NMR spectra of half-integer quadrupolar nuclei via DFS-QCPMG and RAPT-QCPMG pulse sequences. *Chem. Phys. Lett.* **2003**, *379*, 1−10.

(42) Siegel, R.; Nakashima, T. T.; Wasylishen, R. E. Sensitivity enhancement of NMR spectra of half-integer quadrupolar nuclei in the solid state via population transfer. *Concepts in Magnetic Resonance Part A: Bridging Education and Research* **2005**, *26*, 47−61.

(43) Saalwächter, K.; Lange, F.; Matyjaszewski, K.; Huang, C.-F.; Graf, R. BaBa-xy16: Robust and broadband homonuclear DQ recoupling for applications in rigid and soft solids up to the highest MAS frequencies. *J. Magn. Reson.* **2011**, *212*, 204−215.

(44) Hartmann, S. R.; Hahn, E. L. Nuclear double resonance in the rotating frame. *Phys. Rev.* **1962**, *128*, 2042−2053.

(45) Pines, A.; Gibby, M. G.; Waugh, J. S. Proton-enhanced NMR of dilute spins in solids. *J. Chem. Phys.* **1973**, *59*, 569−590.

(46) Bailey, M. The crystal structure of indanthrone. *Acta Crystallogr.* **1955**, *8*, 182−185.

(47) Momma, K.; Izumi, F. VESTA3 for three-dimensional visualization of crystal, volumetric and morphology data. *J. Appl. Crystallogr.* **2011**, *44*, 1272−1276.

(48) Hope, M. A.; Griffith, K. J.; Cui, B.; Gao, F.; Dutton, S. E.; Parkin, S. S.; Grey, C. P. The role of ionic liquid breakdown in the electrochemical metallization of VO_2: an NMR study of gating mechanisms and VO_2 reduction. *J. Am. Chem. Soc.* **2018**, *140*, 16685−16696.

(49) Voskian, S.; Hatton, T. A. Faradaic electro-swing reactive adsorption for CO_2 capture. *Energy Environ. Sci.* **2019**, *12*, 3530−3547.

(50) Ferrara, C.; Dall'Asta, V.; Berbenni, V.; Quartarone, E.; Mustarelli, P. Physicochemical characterization of $AlCl_3$-1-ethyl-3-methylimidazolium chloride ionic liquid electrolytes for aluminum rechargeable batteries. *J. Phys. Chem. C* **2017**, *121*, 26607−26614.

(51) Xu, J. H.; Jadhav, A. L.; Turney, D. E.; Messinger, R. J. Molecular-level environments of intercalated chloroaluminate anions in rechargeable aluminum-graphite batteries revealed by solid-state NMR spectroscopy. *J. Mater. Chem. A* **2020**, *8*, 16006−16017.

(52) Wang, J.; Polleux, J.; Lim, J.; Dunn, B. Pseudocapacitive contributions to electrochemical energy storage in TiO_2 (Anatase) nanoparticles. *J. Phys. Chem. C* **2007**, *111*, 14925−14931.

(53) Schoetz, T.; Gordon, L.; Ivanov, S.; Bund, A.; Mandler, D.; Messinger, R. Disentangling faradaic, pseudocapacitive, and capacitive charge storage: A tutorial for the characterization of batteries, supercapacitors, and hybrid systems. *Electrochim. Acta* **2022**, *412*, 140072.

(54) Wu, Y.; Zeng, R.; Nan, J.; Shu, D.; Qiu, Y.; Chou, S. L. Quinone electrode materials for rechargeable lithium/sodium ion batteries. *Adv. Energy Mater.* **2017**, *7*, 1700278.

(55) Kamath, G.; Narayanan, B.; Sankaranarayanan, S. K. Atomistic origin of superior performance of ionic liquid electrolytes for Al-ion batteries. *Phys. Chem. Chem. Phys.* **2014**, *16*, 20387−20391.

(56) Shi, J.; Zhang, J.; Guo, J. Avoiding pitfalls in rechargeable aluminum batteries research. *ACS Energy Lett.* **2019**, *4*, 2124−2129.

(57) Xu, J. H.; Turney, D. E.; Jadhav, A. L.; Messinger, R. J. Effects of graphite structure and ion transport on the electrochemical properties of rechargeable aluminum-graphite batteries. *ACS Appl. Energy Mater.* **2019**, *2*, 7799−7810.

(58) National Institute of Advanced Industrial Science and Technology (AIST), 1,4,9,10-anthracenetetrol, 10/04/2021, 1999; https://sdbs.db.aist.go.jp/sdbs/cgi-bin/landingpage?sdbsno/17265.

(59) O'Reilly, D. E. NMR chemical shifts of aluminum: Experimental data and variational calculation. *J. Chem. Phys.* **1960**, *32*, 1007−1012.

(60) Kunicki, A. R.; Oriechin, A.; Zachara, J. Reaction of $MeAlCl_2$ with ethyl alcohol (1:1) leading to $[(Cl_2Al)_3(\mu\text{-OEt})_6Al]$. *Main Group Metal Chemistry* **1998**, *21*, 365−370.

(61) Erný, Z.; Macháček, J.; Fusek, J.; Ásenský, B.; Kříž, O.; Tuck, D. G. ^{27}Al NMR studies of the hydrolysis of aluminium(III) chloride in non-aqueous media. *Inorg. Chim. Acta* **2000**, *300−302*, 556−564.